PAPER

A bioinspired apparatus for modeling peristaltic pumping in biophysical flows

To cite this article: R Ibanez and D H Kelley 2022 *Bioinspir. Biomim.* **17** 066023

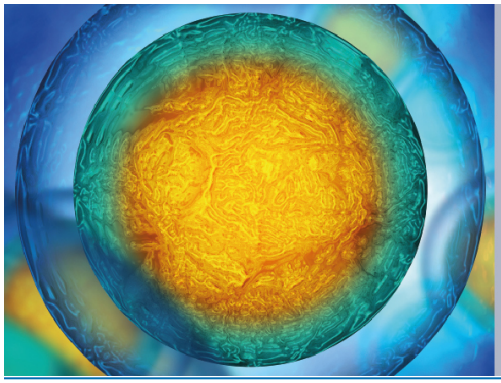

IOP Publishing Bioinspir. Biomim. 17 (2022) 066023 https://doi.org/10.1088/1748-3190/ac9c7e

Bioinspiration & Biomimetics

PAPER

RECEIVED
25 July 2022

REVISED
5 October 2022

ACCEPTED FOR PUBLICATION
21 October 2022

PUBLISHED
4 November 2022

A bioinspired apparatus for modeling peristaltic pumping in biophysical flows

R Ibanez* and D H Kelley

Department of Mechanical Engineering, University of Rochester, Rochester, NY 14627, United States of America
* Author to whom any correspondence should be addressed.

E-mail: ribaneza@rochester.edu

Keywords: biophysics, fluid mechanics, peristaltic pumping, biomimetics

Abstract

In this study, we present a novel, bioinspired experimental apparatus, its construction, data acquisition methodology, and validation for the study of peristaltic flows. The apparatus consists of a series of stepper motor actuators, which deflect a deformable membrane to produce peristaltic flows. We show that this apparatus design has significant advantages over previous designs that have been used to study peristaltic flows by offering a much wider range of modeling capabilities. Comparisons between the capabilities of our apparatus and previous ones show our apparatus spanning a larger range of wavelength λ, wave speed c, amplitude A, and waveform (i.e. the apparatus is not constrained to nondispersive waves or to a sinusoidal shape). This large parameter range makes the apparatus a useful tool for biomimetic experimental modeling, particularly for systems that have complex waveforms, such as peristaltic flows in perivascular vessels, arteries, the cochlea, and the urethra. We provide details on the experimental design and construction for ease of reconstruction to the reader. The apparatus capabilities are validated for a large parameter range by comparing experimental measurements to analytic results from (Ibanez *et al* 2021 *Phys. Rev. Fluids* **6** 103101) for high Reynolds number ($Re > 1$) and (Jaffrin and Shapiro 1971 *Annu. Rev. Fluid Mech.* **3** 3–37) for low Reynolds number ($Re < 1$) applications. We show that the apparatus is useful for biophysical peristaltic studies and has potential applications in other types of studies.

Nomenclature

Symbol	Meaning
A	Wave amplitude
Q	Flow rate
L	Channel gap
Q_o	Dimensionless flow rate
c	Wave speed
ΔP_λ	Mean pressure rise over wavelength
λ	Wavelength
α_T	Thermal diffusivity
α	Wavenumber
T	Temperature
ν	Kinematic viscosity of fluid
ΔT	Temperature difference
ρ	Density of fluid
β	Thermal expansion coefficient
x	Spatial dimension
Ra	Rayleigh number
y	Spatial dimension
$\mathrm{Ra_c}$	Critical Rayleigh number
t	Temporal dimension
S_m	Stepper motor step angle
Re	Reynolds number
T_m	Actuator thread pitch
ϵ	Dimensionless amplitude
δ_y	Actuator minimum displacement
κ	Dimensionless wavelength
δ_e	Discretized displacement error
V_rms	Root-mean-square velocity
g	Acceleration of gravity
δ_BL	Boundary layer length
f_{drv}	Output frequency of microcontroller
$\bar{Q}$	Average flow rate

1. Introduction

Peristaltic flows are produced when a fluid-filled channel with flexible walls is subjected to a traveling, periodic wall deformation. The wall deformation produces a pressure difference in the channel and as such produces a flow. Peristaltic flows are

found in many natural contexts, such as the inner ear [1], urethra [2], brain perivascular spaces [3], and stomach [4]. Peristaltic flows are also utilized in pumping applications where sanitary conditions are required [5] or non-Newtonian fluids are present [6]. Some examples of studies of peristaltic flows for pumping and/or mixing applications can be found in Selverov and Stone [7] and Lozano [2].

The purpose of this paper is to present a bioinspired experimental apparatus design which offers significant advantages over previous designs. Our design was conceived to model flows in the inner ear in mammals, typically driven by quasi-periodic deformations of fluid channel boundaries, which can produce peristaltic pumping. In the inner ear, these peristaltic flows span a wide range of parameters, with various waveforms, frequencies, and amplitudes. As a consequence, the design we present was developed to have the capability of modeling a large span of parameters, with applications beyond the original purpose. Notably, the apparatus allows for a closer reproduction of biophysical conditions of peristalsis. The design is capable of allowing complex waveforms that reflect real-world peristalsis in biological systems. Examples of such complex peristaltic waveforms can be found in many contexts, including artery wall motions that may drive cerebrospinal fluid through the brain [8] and cochlear motions that may maintain homeostasis in the ear's organ of Corti [1].

The paper is divided into the following sections: In section 2, we review the important physical considerations and characteristics of peristaltic flows. In section 3, we review previous approaches and discuss the motivation behind our experimental design. We explain how the design allows for the system to be used in a diverse set of experiments with a wide parameter range. Section 4 includes detailed explanations of the composition of the design and its operation. This section contains the most critical information for the reader to replicate the apparatus. Section 5 is dedicated to validation of the design. We demonstrate that the experiment is capable of accurately modeling peristaltic pumping for different flow regimes, thus making it versatile for future studies.

2. Physics of peristaltic flows

To understand peristaltic flows, consider the simple model in figure 1, which is similar to those used successfully in prior analytic studies [9–11]. A peristaltic flow occurs when the boundary of the channel is deformed in a periodic manner and propagates in one direction. The system can be characterized by a deformation amplitude A, channel gap height L, wave speed c, wavelength λ and wave frequency $\omega = 2\pi c/\lambda$. We adopt Cartesian coordinates (x, y) as shown and denote time t.

The deformation of the boundary is given by the function $\eta(x,t)$, which describes how the boundary is deflected in the y direction, normal to the boundary itself. Consider the simple case of a traveling sinusoidal wave, described as $\eta(x,t) = A\sin(\alpha x + \omega t)$, where $\alpha = 2\ \pi/\lambda$. Note that peristalsis is not restricted to a sinusoidal η function, but we restrict ourselves in this section for simplicity in understanding the problem. The boundary at $y = 0$ is stationary, while the boundary at $y = L$ is deformed such that it can be described as $y_\Omega = L + \eta(x,t)$. This continuous change in the boundary forces fluid to be displaced and creates a peristaltic flow

$$\frac{\partial \vec{U}}{\partial t} + \vec{U}\cdot\nabla\vec{U} = -\frac{\Delta P}{\rho} + \nu\nabla^2\ \vec{U} \qquad (1)$$

where $\vec{U} = [u(x,y), v(x,y)]$ is the flow velocity, such that u is the velocity of the flow in the x direction and v is the velocity of the flow in the y direction, ν is the kinematic viscosity of the fluid, ρ is the density of the fluid, and P is the pressure field. The relevant boundary conditions to achieve peristaltic pumping include periodic boundary conditions at the ends of the channel,

$$u(0,y) = u(\lambda,y), v(0,y) = v(\lambda,y),$$

no slip boundary conditions at the solid boundaries,

$$u(0,x) = v(0,x) = u(x,L) = 0,$$

and the moving boundary condition,

$$v(x,L) = \frac{\partial \eta(x,t)}{\partial t}.$$

The conditions may vary slightly depending on the intended peristaltic pumping model.

Jaffrin and Shapiro [12] showed that the key parameters that determine peristaltic flow characteristics are the Reynolds number

$$\mathrm{Re} = \frac{cL^2}{\nu\lambda},$$

the amplitude ratio

$$\epsilon = \frac{A}{L},$$

the wavenumber (which also represents a ratio between the channel gap height and wavelength of the deformation)

$$\kappa = \frac{\lambda}{L},$$

and the dimensionless time-mean flow rate

$$Q_o = \frac{\bar{Q}}{Lc},$$

where $\bar{Q}$ is the time averaged volume flow rate in the x-direction. Our experimental design has greater flexibility in modeling the key parameters of Re, ϵ and α

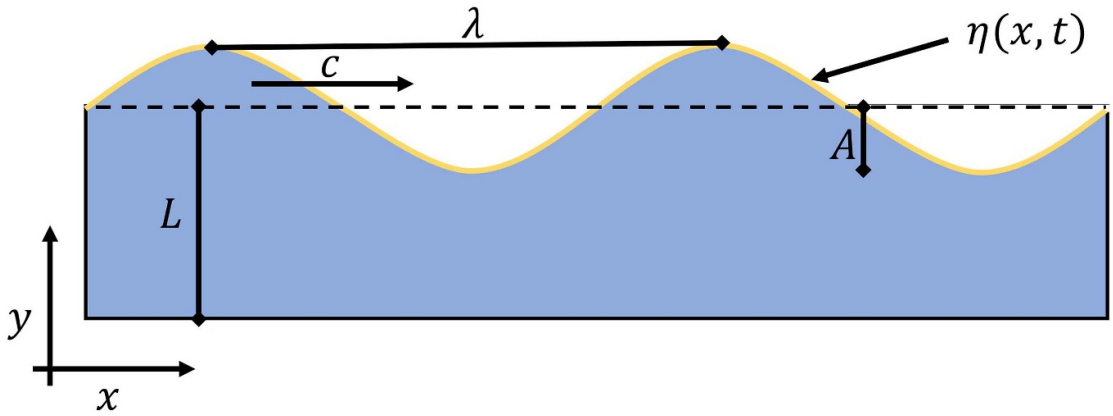

Figure 1. A simplified view of a peristaltic system. Blue indicates the fluid. Yellow is the flexible wall. x and y are spatial coordinates. A is the amplitude of deformation. L is the channel gap height. c is the wave speed and λ is the wavelength of the deformation. $\eta(x,t)$ is a function which describes the position in y of the flexible wall (yellow).

when compared to previous studies. These enhanced capabilities are discussed in detail in section 3.1.

The boundary conditions at the ends of the channel influence a peristaltic flow strongly. For example, end boundary conditions can be changed by imposing a net pressure difference between the two ends of the channel, which alters the resulting flow. We denote the mean pressure rise over one wavelength (assuming that pressure is only a function of t and x) as ΔP_λ. When the setup is connected to two independent reservoirs at each end, it follows that a mean pressure gradient will be created between the two reservoirs if pumping occurs. However, if both ends of the device are connected to each other, in a recirculating manner, the mean pressure gradient must be zero. Previous authors denoted this the condition of 'zero pressure rise' [12–14]. The recirculating setup effectively emulates an infinite train of waves; thus the flow is always 'pumping' in the same way as if the pump were displacing fluid from a lower reservoir to an outlet at a greater height than the rest of the system. Different flow rates are to be expected if a mean pressure condition is imposed on the system.

3. Design motivation

3.1. Previous designs

Researchers constrain their systems to parameter ranges relevant to the problems of their interest. While this is a reasonable approach for studying a specific phenomenon, it comes at the cost of limiting the experimental ability to finely adjust parameters and perform large parameter scans over wavelength, frequency, or amplitude. Reviewing previous experimental designs is a useful exercise in determining how design decisions can limit studies.

Jaffrin and Shapiro [12] used a series of rotating rollers around a channel to study peristaltic flows. A design schematic can be seen in figure 2(a). The system design consisted of a series of rollers that were placed around a cylinder where each roller made contact with the flexible membrane and was given a set actuation length. The actuation length of the rollers could be manually adjusted to alter the amplitude and wavelength in the apparatus. As the cylinder rotated, it displaced a flexible membrane such that it induced a peristaltic motion on the channel with the configured waveform. The adjustment required mechanical adjustment of the setup each time either amplitude, waveform, or wavelength was varied. The parameter range they were able to model spanned a wave speed between 1–6 cm s^{-1}, a wavelength of $1L$–$30L$, and an amplitude ratio of 0.33–0.70. Their goal was to develop a model for peristaltic flows with low to moderate Reynolds number ($Re < 60$) and long wavelength $\kappa \gg 1$.

Yin and Fung [15] used a belt setup on a channel. A design schematic can be seen in figure 2(c). The belt was positioned so its teeth displaced the flexible membrane of the channel as the belt was moved. This severely limited the ability to test different amplitudes, wavelengths, and waveforms, as the parameters were tied to the belt teeth and size. Frequency was adjustable by varying the speed at which the belt was displaced, but any other parameter changes required the belt to be changed. The parameter range they were able to model spanned a wave speed between 0.03–0.18 mm s^{-1}, a wavelength of $2.2L$–$2.4L$, and an amplitude ratio of 0.3 and 0.4. Their goal was similar to [12]; they sought to characterize the basics of peristaltic flows with an emphasis on biological systems. While they did not explicitly dictate the parameter range of their analytic modeling, it is stated validation is limited to and long wavelengths $\kappa \gg 1$. Only a small amplitude $\epsilon \ll 1$ is strictly stated as a criterion. A similar setup was used by [7]. A design schematic can be seen in figure 2(d). They used a belt setup, but their experiment was completely enclosed, which means there was no reservoir or outlet for the fluid.

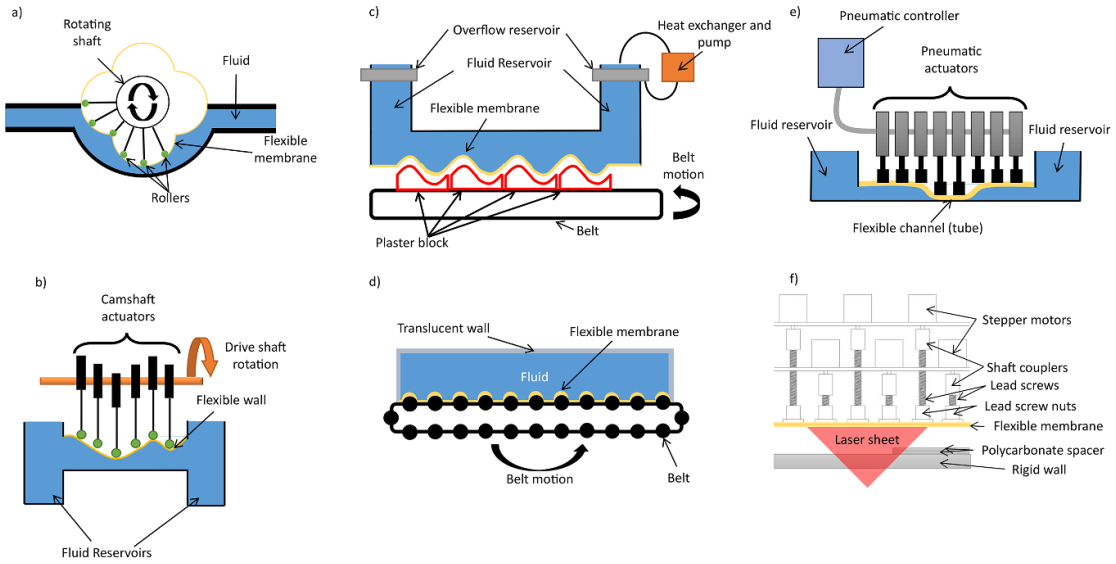

Figure 2. Design schematics from different studies. (a) Weinberg *et al* [11]. (b) Ayukawa *et al* [16]. (c) Yin and Fung [15]. (d) Selverov and Stone [7]. (e) Lozano [2]. (f) This study.

Ayukawa *et al* [16] used a camshaft which displaced a flexible wall. A design schematic can be seen in figure 2(b). The camshaft operated in a similar fashion to that of a combustion engine. The cams themselves actuated a rod which in turn displaced the flexible membrane. The system was particularly limited by the fact that mechanical components had to be swapped to adjust the parameters of the system. The only parameter that could be easily adjusted is the frequency as the speed of rotation was simply adjusted by the camshaft motor. The parameter range they were able to model spanned a wave speed between 4 and 8 cm s^{-1}, a wavelength of 4.8L–17L, and an amplitude ratio between 0.19–0.69. Their goal was to study and develop a model for peristaltic flows at high Reynolds number Re $\gg 1$ and long wavelength $\kappa \gg 1$.

Lozano [2] used a series of pneumatic actuators which compressed a flexible tube and induced a peristaltic flow. A design schematic can be seen in figure 2(e). The main limitation in the system was the use of pneumatic actuators which are limited in their range of motion. This severely limited the range of parameters that can be modeled. The parameter range this study was able to model spanned a wave speed between 1.2 and 3.6 cm s^{-1}, a wavelength of 1L–12L, and an amplitude ratio of 1. The experiment was used to study transport effects in the parameter range of the human urethra. The flows studied generally fell in the category of low Reynolds number Re < 1, large amplitude $\epsilon \approx 1$ and long wavelengths $\kappa \gg 1$.

These previous studies serve as highlights of the large body of experimental peristaltic flow research. A comparison of parameter ranges between experiments can be found in table 1. There is diversity in the design choices, and here we offer a design that is capable of modeling the large range of parameters found in previous works in one system. Our design was inspired by analyzing previous experiment designs, which appear to mainly have used two notable design approaches. The first approach relies on a continuous mechanical component to deform the flexible membrane. This means that whatever component is used to actuate the wall has a continuous shape over the length of the experimental channel. The other approach uses discrete deformation locations. An example of the first approach is a continuous belt where the bumps of the belt deform the channel and induce a flow. An example of the second approach is using a series of actuators placed next to each other in an array to deform the wall at discrete points. As mentioned in the description of previous studies, other experiments have limitations in the parameter range they are capable of modeling. While some adjustability is available, often it involves changing the apparatus' components or requires a complete redesign. Our system design is capable of adjusting the following parameters with no hardware changes: The wavelength, wave frequency, amplitude (though large changes require minor hardware adjustment), and waveform. Additionally, our

Table 1. A comparison of modeling capabilities of previous experiments.

Reference	c (mm s^{-1})	λ/L	ϵ
Jaffrin and Shapiro [12]	10–60	1–30	0.33–0.7
Yin and Fung [15]	0.03–0.18	2.2 or 2.4	0.3 or 0.4
Ayukawa *et al* [16]	40–80	4.8–17	0.19–0.69
Lozano [2]	12–36	1–12	1

approach allows us to model dispersive waves and even non periodic deformations.

The key component that differentiates our design is that by using stepper motors and high-pitch lead screws as actuators, we can overcome the deficiencies of the discrete approach used in previous studies. It allows a user to finely control the motion of each actuator and as such determine the speed and position of displacement at each point in the system with high precision, independently. To quantify the advantages of our apparatus, consider the parameter range available to our chosen hardware configuration. We are able to span the following parameter range: λ from 5.08 cm to 60.96 cm, ϵ up to 0.8 and c up to 5 m s^{-1}. From table 1, it is clear that our experimental system has significantly broader capabilities than previous systems. Further details on our apparatus' limitations and what dictates those limitations is discussed in the next section 4.

4. Experimental design

In this section, we describe the experimental design in detail and the reasoning behind the design choices. The goal is to provide the reader with the information needed to construct an apparatus, adjust as needed, and operate the apparatus. We separate the discussion into three parts: hardware, controls, and data acquisition. Importantly, the hardware section will provide the reader with information on the strictest limitations of our apparatus' parameter range, those due to design characteristics.

4.1. Hardware

The design of our apparatus consists of a square channel to be filled with fluid, where one of the walls is flexible. The flexible wall is needed in order to allow deformation of the channel. The dimensions of the channel are 2.54 cm $\times$ 2.54 cm $\times$ 91.4 cm. The rigid walls are made of transparent polycarbonate, while the flexible wall is neoprene rubber. The flexible wall is deformed by an array of actuators bolted above the flexible wall. Figure 3 shows a diagram of the experiment where the array of actuators is visible. The actuators are stepper motors (Pololu Bipolar NEMA 13 10 V 0.5 A/phase), each of which drives a threaded shaft in a nut that displaces the membrane. The ends of the channel are connected to flexible tubing. The tubing is connected to separate reservoirs at each end, or alternatively, each end is connected to a T-junction and a single reservoir.

The configuration of the reservoirs affects the boundary conditions. Depending on the configuration, the induced peristaltic flow will change, as it affects the mean pressure rise, which is discussed in section 2.

To use the stepper motor approach for actuation, one must consider that the motors rotate in a discrete manner (steps). The motors rotate at an angle S_m with each step. For our motors, $S_\mathrm{m} = 1/200$ rev. The step angle is dictated by the properties of the motor, and it is possible to use stepper motor drivers which allow for micro-stepping, which decreases the step angle. For example, using a stepper driver in quarter stepping mode would mean that a motor moves an angle of $S_\mathrm{m}/4$ with each step. Thus, micro-stepping increases the resolution of the rotation and can reduce vibrations during operation. However, a limiting factor to consider is the speed of impulses that must be sent to induce motion, which may exceed the capabilities of a microcontroller used to control the motors. In general, smaller steps mean higher resolution and smoother motion at the cost of the potential maximum speed of the motor. The parameter range the apparatus can model is closely tied to the stepper motor characteristics; thus they are an important to consider during planning and construction.

As figure 3 shows, in our device, each stepper motor (controlled using a Pololu DRV-8834 stepper driver) is connected to a threaded shaft (Igus with threads DS6.35 $\times$ 25.4) via a shaft coupler. The shaft is then connected to a special nut (Igus DST-JFRM-C-01-DS6.35 $\times$ 25.4), which is glued onto the flexible membrane. The shaft's thread pitch T_m, together with S_m, dictates the minimum distance a stepper motor can displace the flexible membrane. For example, with $S_\mathrm{m} = 1/200$ rev and $T_m = 2.54$ cm rev^{-1} (as in our device), the minimum displacement is $T_m S_\mathrm{m} = 0.127$ mm. Therefore, the smallest wave amplitude that can be modeled is $S_\mathrm{m} T_m$. The minimum wavelength that can be modeled is dictated by the distance between actuators. In our experimental setup, the distance between motors is 2.54 cm, which means the minimum wavelength that can be modeled is 5.08 cm, according to the Nyquist criterion. Longer wavelengths can be modeled with greater fidelity. In order to decrease the distance between motors, we used a stacking arrangement as shown in figure 3. Stacking is needed so that the motor casing of neighboring motors does not block the shaft.

A simple and useful hardware adjustment can be performed by inserting sheets of transparent polycarbonate into the channel. The purpose of these sheets is to change the channel gap height L. Adjusting the channel gap height has three effects: The Reynolds number can be adjusted as L changes, the range of amplitudes that can be produced with accuracy in the system is greater when the gap is smaller, and the aspect ratio κ depends on L. Smaller channel gaps, however, reduce visibility and can make accurate flow measurements more difficult. We use 0.318 cm sheets of polycarbonate in our setup and stack them. With no inserts, the channel gap height is $L = 2.54$ cm. With inserts, we can reduce the gap size to 0.318 cm. This allows us to reduce the Reynolds number in some of our measurements, as well as

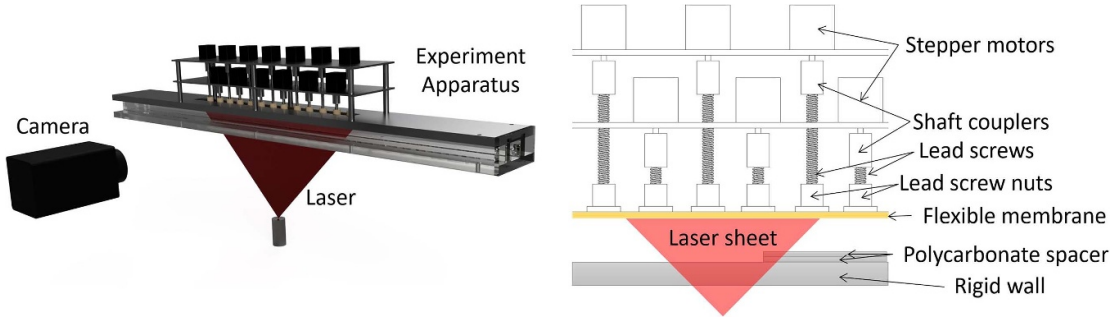

Figure 3. Left: rendering of the key components of the experimental setup. Right: design images of the experimental setup. The side view matches the perspective of the simplified model in figure 1.

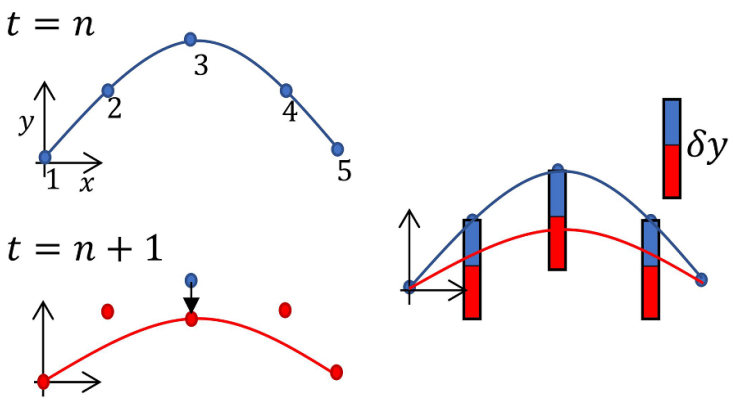

Figure 4. Visual representation of the procedure for discretizing the idealized continuous wave to a form that stepper motors can use. The red and blue curves are idealized wall positions. The circles represent the position of the ith stepper motor. The middle image shows the calculation to determine if a step must be made between two points in time n and $n+1$.

increase the amplitude ratio. When the effective gap size is decreased, it means that the actuators can produce a higher amplitude ratio ϵ even while traveling shorter distances.

The channel is filled with water, and to visualize its motion, we introduce microspheres with a diameter between 100 and 116 μm (Cospheric). The techniques for obtaining flow data through the visualization of particles are covered in the section 4.3.

4.2. Controls

To produce a traveling wave wall deformation for a peristaltic flow in the experimental setup, we use a MATLAB code to determine the necessary motion for the array of stepper motors. The stepper motors must rotate in a specific manner to replicate the desired wave wall deformation as closely as possible. The MATLAB code that determines this motion is accessible in the following [17]. In the MATLAB code, the desired wall deformation is specified as a function of x and t, for example $\sin(\alpha x - \omega t)$. This analytic function is defined as the idealized displacement of the wall $\eta(x,t)$. The MATLAB algorithm uses the motor hardware parameters S_m and T_m and the idealized displacement to calculate the necessary motions to model the idealized wave. Figure 4 illustrates the algorithm that determines the motion.

To understand the operation and limitations of the procedure shown in figure 4, consider the ith stepper motor to be located on the flexible wall at position x_i. Each motor can displace the flexible wall a discrete position, by a distance $\eta_i(x_i,t)$. The stepper motors have discrete motions with minimum displacement $\delta y = S_\mathrm{m} T_m$. In order to simulate a continuous deformation of the wall in the apparatus, the MATLAB code calculates the motion required by each motor by taking the error between the idealized function $\eta(x,t)$ at the upcoming time t_1 and the motor's current deflection at the current time t_0. The scale of the discrete time is dictated by the signal output rate of the hardware (Arduino MEGA2560 R3 in our case). For example, if the controller output signals at a rate of 2 kHz, then the time scale is equal to 500 μs. The error is calculated by

$$\delta_e = \eta(x,t_1) - \eta(x,t_0). \tag{2}$$

Now the MATLAB algorithm determines that, if δ_e is larger than half the minimum displacement, i.e. $|\delta_e| > \delta y/2$, then a step output is produced with the according direction to minimize the error. For example, in the case of δ_e being positive, the algorithm determines

a step in the negative direction must be taken. Otherwise, no step is produced as the current location is where the error is minimized. The MATLAB code uses equation (2) at each point in time to produce a text file that contains the motion information for the stepper motors. The text file is then used in a Python code that controls the stepper motors via the MEGA2560 Arduino R3 board. The Python code can be found in the following repository [18]. A visual illustration of the idealized wave to apparatus motion process is shown in figure 4.

An idealized wave where $\partial\eta(x,t)/\partial t > S_{\mathrm{m}} T_m f_{drv}$, where f_{drv} is half the maximum output frequency of the controlling hardware, will not be able to be modeled exactly. Additionally, the amplitude of the idealized wave must be at least larger than the minimum amplitude, i.e. $\eta(x,t) > S_{\mathrm{m}} T_m$. The idealized wave must be described as a function of x and t.

4.3. Data acquisition

To perform velocity field measurements in the apparatus, we use particle imaging velocimetry (PIV) and particle tracking velocimetry (PTV) techniques. To illuminate the microspheres in the fluid we use a 5 mW, 632 nm laser with a line lens, which shines through the wall opposite the flexible membrane. To capture video of the flow, we use an Emergent 4000 M camera. Most videos are PIV with the MATLAB version of the open-source code PIVlab [19]. In the case of Particle Tracking we use a MATLAB code, PredictiveTracker, which is described in Kelley and Ouellette [20]. Figures 5 and 6 were produced using PIV, whereas figures 7 and 8 were produced using PTV.

4.4. Data processing

PIVlab can produce a velocity field for each frame that is captured. We recommend a frame rate that is an integer multiple of the flow frequency. For example, if the induced peristaltic flow has a frequency of 2 Hz, we recommend that captured video is at a multiple of 2 Hz. A good guideline for determining the desired minimum frame rate is to plot a discretized version of the forcing function with a sampling rate equivalent to the frame rate. If the data appears too coarse, the frame rate should be increased if possible. Additional information on PIV techniques can be found in [21, 22]. When studying periodic flows, phase averaging PIV measurements can produce velocity fields of high quality by combining measurements made at similar phases in the periodic flow cycle, over many cycles. This produces a smoothed velocity field from the periodic data.

For high Reynolds number flows, the boundary layer is small. From Ibanez *et al* [10] we can estimate the boundary layer length to be $\delta_{\mathrm{BL}} = \sqrt{2\nu\omega^{-1}}$, making the boundary layer difficult to visualize unless one focuses measurements on the region. The top region of our experiment can be particularly difficult to visualize in PIV since the flexible boundary enters the interrogation area, though one can track the boundary deformation if desired. For measurements in the bulk region, we find that neglecting the top and bottom boundaries can help with data processing at high Reynolds number since the flow shows little dependence on y. For our measurements of the bulk flow we restricted measurements to the section where $0.05L < y < 0.9L$.

4.5. Thermal considerations

For low Reynolds number applications of our apparatus, it is important to consider the potential for a background flow induced by thermal convection in the system. We can estimate the thermal stability of the apparatus by defining the Rayleigh number to be $\mathrm{Ra} = g\beta\nu^{-1}\alpha_{\mathrm{T}}^{-1}(\Delta T)L^3$, where T is the temperature, ΔT is the temperature difference, g is the acceleration of gravity, β is the thermal expansion coefficient, and α_T is the thermal diffusivity of the fluid. The critical Rayleigh number for the onset of convective flow in a two dimensional idealized system similar to our apparatus is $\mathrm{Ra_c} = 1708$ [23], which suggests that the thermal gradient required to destabilize our apparatus is of the magnitude of 1 mK. Though ambient temperatures may be reasonably stable, control as fine as 1 mK is rare. Thus, it becomes important to measure the background convection to know how our measurements can be affected. For our apparatus, we measured the maximum speed of background convection to be 0.1 mm s^{-1}. For experimental measurements, one should take into account that if the induced peristaltic flow is of a similar magnitude, the measurements can be greatly affected. If slower flow speeds are required for modeling, one can consider changing the fluid and/or the gap size L.

5. Experiment validation

In this section, we present validation of the experimental design for a selection of diverse parameters to demonstrate versatility. The validation is split into two subsections consisting of high Reynolds number ($\mathrm{Re} > 1$) validation and low Reynolds number ($\mathrm{Re} < 1$) validation since the device's channel gap height L is different for each and analytic theories we use for validation are limited by Reynolds number. Additional validations were published previously [10].

5.1. High Reynolds number validation

For the validation of high Reynolds number flows, we compare measured data from the experiment against analytic results derived from the formulation in Ibanez *et al* [10]. Experimental data is acquired using PIV measurements according to the procedures detailed in section 4. One of the main advantages of our system over previous ones is the ability to model any kind of waveform. Examples include traveling sine waves, traveling Gaussian waves, and

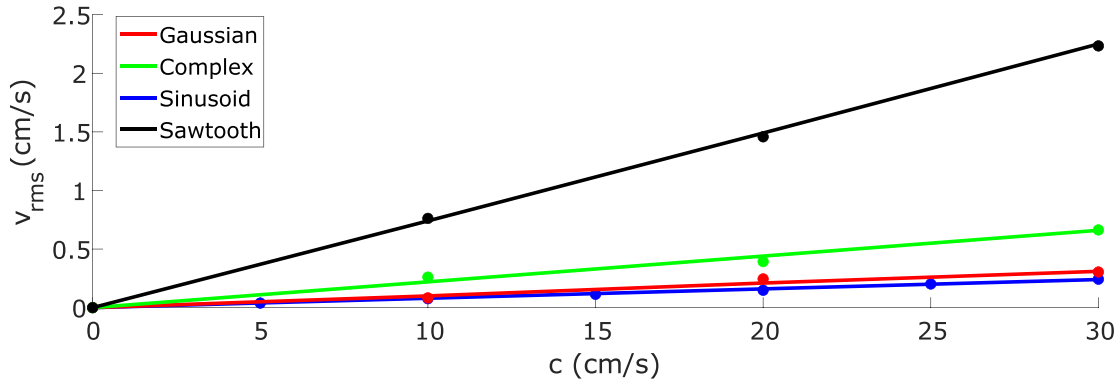

Figure 5. Comparison of experimentally measured V_{rms} (dots) with analytic estimates (lines). Each color represents a different waveforms as referenced in the legend.

square waves. In order to demonstrate the ability to accurately model peristaltic flows, we measure the average bulk velocity for various waveforms and compare to analytic results from Ibanez *et al* [10]. The analytic model does not allow us to compare to dispersive waves, though the experimental setup can produce them. Additionally, we present particle tracking measurements to demonstrate that the transport characteristics of peristaltic flows are modeled accurately.

First, we show experimental validation using the root-mean-square velocity of the flow, $V_{\text{rms}} = (\overline{u^2 + v^2})^{1/2}$, where u is the velocity in the x-direction, v is the velocity in the y-direction, and the overline is the spatiotemporal average over the bulk region of the flow, which is defined as $0.05L \leqslant y \leqslant 0.9L$. Figure 5 shows the comparison of the root-mean-square velocity of waveforms and parameters. We find good agreement between the analytic and experimental results. We determined the goodness of fit to the analytically predicted values and found $R^2 = 0.99$.

We can compare the features of different waveforms by comparing data between analytic and experimental results of the bulk average velocity over time. The bulk average velocity is obtained by phase averaging the experimental measurements and then averaging over space in the channel gap height direction. Details on phase averaging are in section 4.4. Figure 6 compares analytic results and experimental measurements.

It may also be of interest to study Lagrangian dynamics of the flow. We demonstrated in Ibanez *et al* [10] that it is possible to perform high quality PTV measurements to obtain particle paths, which match analytic and numerical estimates. Figure 7 shows a comparison of analytic and experimental Lagrangian results, i.e. particle paths. The effects of different waveforms are evident and can have an impact on mass transport. There are deviations in the analytic and experimental results which are likely due to the differences from the analytic model to the experimental apparatus. Paths recorded in experiments are unevenly distributed because they track actual particles in the apparatus and thus begin at arbitrary locations. Still, it is clear that waveform shape plays a key role, since paths are qualitatively different when forced by Gaussian waves than when forced by sinusoidal motions, in both analytic and experimental results. While these measurements are restricted to producing flows with no net flow rate, it is important to note that the pumping characteristics have been shown to be affected by waveforms as shown in [24]. Although the results are focused on larger amplitude peristaltic pumping, in the case of small amplitude peristaltic pumping, it leaves an open question as to how Lagrangian transport, a key characteristic in microfluidic mixing as shown in [10], is affected by different waveforms.

5.2. Low Reynolds number validation

For the validation of low Reynolds number flows, we compare our experimental results with the analytic analysis from Jaffrin and Shapiro [12]. To prepare the system for low Reynolds number flows, we use polycarbonate inserts to reduce the effective channel gap height L to 0.318 cm. As a consequence, we also increase the accessible range of amplitude ratios, since smaller stepper motor motions can achieve larger amplitude ratios. For the low Reynolds number validation, we use flows with amplitude ratios of $\epsilon = 0.35, 0.4, 0.5, 0.55, 0.6$ and 0.68 and Reynolds numbers 0.05, 0.1 and 0.2.

Previous studies, such as Shapiro [25], Jaffrin and Shapiro [12], Burns and Parkes [26], noted that for low Reynolds number one can expect to find a simple relationship between the nondimensional flow rate Q_o and the amplitude ratio. From the derivation found in Weinberg *et al* [11], as well as in Eckstein [13] we obtain the following relationship:

$$Q_o = \frac{3\epsilon}{2 + \epsilon^2}. \tag{3}$$

Equation (3) is exclusive to the case of zero mean pressure rise, and can be derived from the governing

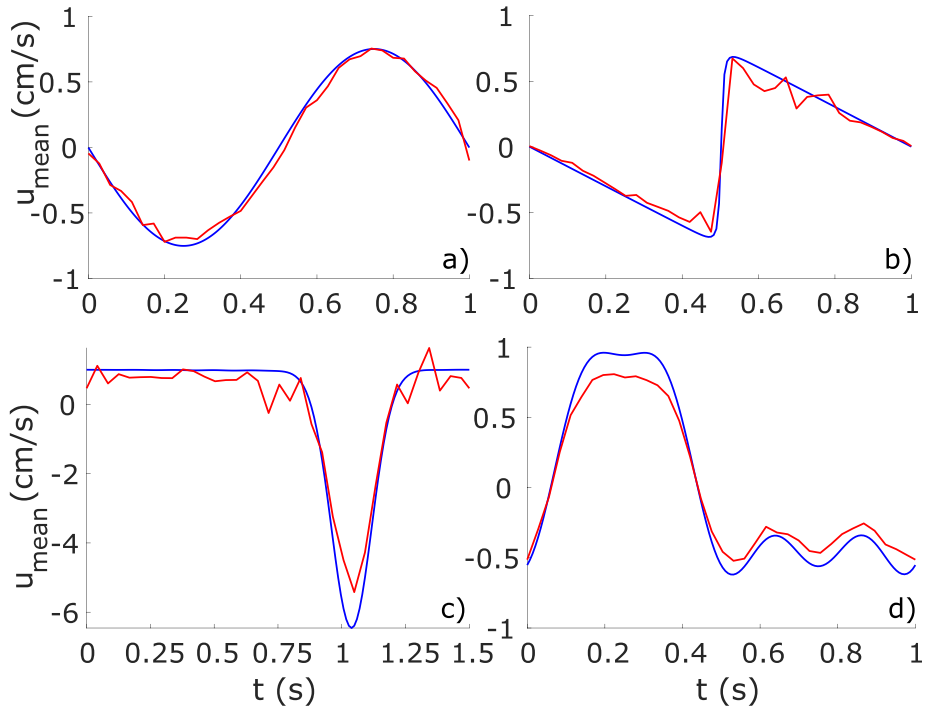

Figure 6. Average bulk flow velocity in the downstream direction for various deformation waveforms including sinusoid (a), sawtooth (b), Gaussian (c), and complex wave (d). Blue curves show analytic estimates derived using the model from Ibanez *et al* [10]. Red curves show experimentally measured values.

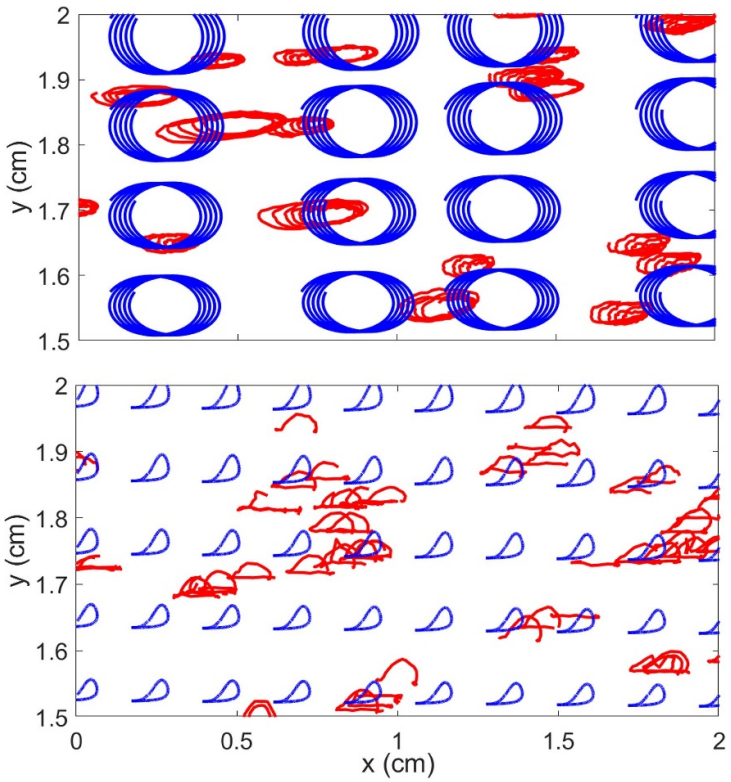

Figure 7. Pathlines in flows driven by wall deformations in the form of traveling sinusoids (left) and Gaussian waves (right). The red curves show experimental measurements, and blue curves show analytic predictions.

equation (1) by assuming the Reynolds number to be low. As discussed in section 2, this means that the apparatus must have a recirculating setup, i.e. one end of the apparatus is connected to the other. Equation (3) provides a single number for validating experimental measurements. In figure 8 we compare

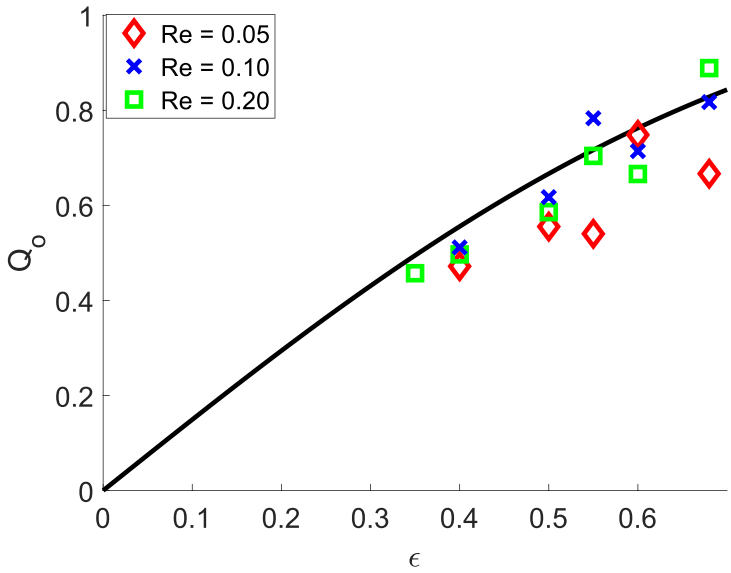

Figure 8. The measured dimensionless flow rate varies with deformation amplitude in close agreement with the prior analytic estimates found in [12] (black curve). Note that these results are exclusive to the recirculating setup, i.e. a zero mean pressure rise.

experimentally measured nondimensional flow rates with the analytic estimates from equation (3) and find good agreement for different values of Re and ϵ. We determined the goodness of fit to the analytically predicted values and found $R^2 = 0.58$. However, if we exclude the two biggest outliers, $R^2 = 0.79$. The nondimensional flow rate also shows how larger amplitudes lead to stronger pumping. Because Weinberg *et al* [11] considered only sinusoidal deformations, this validation is specific to that case.

6. Conclusions

We have described and validated an experimental design for the study of peristaltic flows which can access a wider range of parameters than previous designs. Given its ability to produce a wide range of waveforms, the apparatus has novel potential for biomimetics applications, more accurately replicating conditions in biophysical systems. The versatility of the system allows for future stability studies to be performed, in cases where it is unclear what characteristics are required to cause the flow to become unstable.

The following are suggestions for readers interested in improving on our design. Our apparatus has a square channel, which means that the side walls induce a shear that is not captured by two dimensional models. As Weinberg *et al* [11] pointed out, it is possible to apply corrections to analytic models to account for side wall shear, but if the effect is to be minimized one should separate the distance of the side walls as far as possible.

In the future we hope to use this apparatus for obtaining stability measurements, fully characterize Lagrangian transport at a wider range of parameters, study the effect of disperse waves such as those found in the cochlea [27], and study how dispersive wave peristaltic flows can differ from nondispersive wave peristaltic flows. We would also like to explore the effect of peristalsis under different end boundary conditions, considering Selverov *et al* [7] whose system is a closed box, i.e. no inlet or outlet, and Shokrian *et al* [1] whose system has one closed end and one inlet/outlet.

In this study we validated our experiment for biomimetic applications by ensuring that complex waveforms are captured accurately over a large parameter range. The apparatus was validated for a parameter range that includes flows in complex biological systems. The methods we present provide future opportunities to experimentally study poorly understood flows such as those in perivascular spaces [8] and experimentally analyze the pumping effects of waveforms in biological and industrial peristaltic pumping systems, as suggested by Walker and Shelley [24], whose modeling was limited to analytic and numerical approaches only.

The flexibility of our apparatus allows future experiments in other complex peristaltic pumping cases where they previously were not possible. For example, the ability to model arbitrary waveforms would allow for experimental validation of studies such as Walker and Shelley [24], Liron [28], and Tripathi *et al* [29]. The large parameter range and adjustability of our design can allow for experimental validation of models such as Bhandari *et al* [30] and Afzal and Akram [31].

It is our hope this design will see future use beyond our specific interests. Given the ability to span large parameter sets and arbitrary waveforms we see other research groups can use the tools we provide

(our design and software [17, 18]) for the validation of their own numerical and analytic studies which have not seen experimental results, such as the ones references in section 1.

To conclude, the versatility and simplicity of this experimental design allows for various studies to be done with high cost effectiveness. The same apparatus may be used in completely different studies of peristaltic flows while yielding accurate results.

Data availability statement

The data that support the findings of this study are available upon reasonable request from the authors.

Acknowledgments

The authors wish to thank Ernesto Sanchez for his assistance in developing the control systems for the experiment. This work was supported by the National Science Foundation under Award Number CBET-1552182 and US Army Research Office Grant MURI W911NF1910280.

Author contributions

All authors contributed to the design and construction of the experiment.

Conflict of interest

The authors declare that they have no conflict of interest.

ORCID iD

R Ibanez https://orcid.org/0000-0002-6980-765X

References

[1] Shokrian M, Knox C, Kelley D H and Nam J H 2020 *Sci. Rep.* **10** 1–10
[2] Lozano J N J 2009 Peristaltic flow with application to ureteral biomechanics *PhD Dissertation* University of Notre Dame
[3] Wang P and Olbricht W L 2011 *J. Theor. Biol.* **274** 52–57
[4] Alokaily S, Feigl K and Tanner F X 2019 *Phys. Fluids* **31** 103105
[5] Pozrikidis C 1987 *J. Fluid Mech.* **180** 515–27
[6] Ellahi R, Hussain F, Ishtiaq F and Hussain A 2019 *Pramana* **93** 1–9
[7] Selverov K P and Stone H A 2001 *Phys. Fluids* **13** 1837–59
[8] Mestre H, Tithof J, Du T, Song W, Peng W, Sweeney A M, Olveda G, Thomas J H, Nedergaard M and Kelley D H 2018 *Nat. Commun.* **9** 1–9
[9] Shapiro A H, Jaffrin M Y and Weinberg S L 1969 *J. Fluid Mech.* **37** 799–825
[10] Ibanez R, Shokrian M, Nam J H and Kelley D H 2021 *Phys. Rev. Fluids* **6** 103101
[11] Weinberg S L, Eckstein E C and Shapiro A H 1971 *J. Fluid Mech.* **49** 461–79
[12] Jaffrin M Y and Shapiro A H 1971 *Annu. Rev. Fluid Mech.* **3** 3–37
[13] Eckstein E C 1970 Experimental and theoretical pressure studies of peristaltic pumping *PhD Thesis* Massachusetts Institute of Technology
[14] Jaffrin M and Shapiro A 1971 *Annu. Rev. Fluid Mech.* **3** 13–37
[15] Yin F and Fung Y 1971 *J. Fluid Mech.* **47** 93–112
[16] Ayukawa K, Kawai T and Kimura M 1981 *Bull. JSME* **24** 948–55
[17] Ibanez R 2022 Stepper motor peristaltic motion (available at: https://github.com/NavierAndStokes/peristaltic-motion)
[18] Sanchez E 2022 Mega2560realtimesteppercontroller (available at: https://github.com/Mikwind/Mega2560RealtimeStepperController)
[19] Thielicke W and Stamhuis E J 2014 *J. Open Res. Softw.* **2** e30
[20] Kelley D H and Ouellette N T 2011 *Am. J. Phys.* **79** 267–73
[21] Wilkinson K C 2014 A kinematic and kinetic analysis of a frog launching from water using digital particle image velocimetry *PhD Thesis* Northern Arizona University
[22] Adrian R J 1991 *Annu. Rev. Fluid Mech.* **23** 261–304
[23] Drazin P G and Reid W H 2004 *Hydrodynamic Stability* (Cambridge: Cambridge University Press)
[24] Walker S W and Shelley M J 2010 *J. Comput. Phys.* **229** 1260–91
[25] Shapiro A H 1967 Pumping and retrograde diffusion in peristaltic waves *Proc. Workshop Ureteral Reflux Children, Nat. Acad. Sci. (Washington, DC)*
[26] Burns J and Parkes T 1967 *J. Fluid Mech.* **29** 731–43
[27] Edom E 2013 Fluid flow in the cochlea: numerical investigation of steady streaming and rocking stapes motions *PhD Thesis* ETH Zurich
[28] Liron N 1976 *Bull. Math. Biol.* **38** 573–96
[29] Tripathi D, Narla V and Aboelkassem Y 2020 *Phys. Fluids* **32** 082004
[30] Bhandari D, Tripathi D and Narla V 2020 *Int. J. Mech. Sci.* **188** 105949
[31] Afzal Q and Akram S 2021 *J. Therm. Anal. Calorimetry* **143** 2291–312